Journal of Magnetic Resonance **150,** 147–155 (2001)
doi:10.1006/jmre.2001.2323, available online at http://www.idealibrary.com on IDEAL®

Imaging the Long-Range Dipolar Field in Structured Liquid State Samples

R. Bowtell, S. Gutteridge, and C. Ramanathan

Magnetic Resonance Centre, School of Physics and Astronomy, University of Nottingham, University Park, Nottingham, NG7 2RD, United Kingdom

Received September 29, 2000; revised March 9, 2001; published online May 10, 2001

We describe imaging experiments in which the pattern of the dipolar field generated by spatially modulated nuclear magnetization is directly visualized in simply structured phantoms. Two types of experiment have been carried out at 11.7 T using ^{1}H NMR signals. In the first, the field from a single spin species is imaged via its own NMR signal. In the second, the NMR signal from one spin species is used to image the field generated by a second species. The field patterns measured in these experiments correspond well with those calculated using simple theoretical expressions for the dipolar field. The results also directly demonstrate the spatial sensitivity of the signal generated using dipolar field effects, indicating that the range of the field depends upon the inverse of the spatial frequency with which the magnetization is modulated.

Key Words: **MRI; dipolar field; intermolecular multiple-quantum coherences.**

INTRODUCTION

The dipolar magnetic field generated by nuclear magnetization is generally neglected in NMR experiments. However, in highly polarized samples this field can have a significant effect on the evolution of the magnetization, giving rise to multiple spin echoes (*1–4*) and unexpected multiple quantum coherences (*5, 6*) between spins which are found in different molecules. These effects are most strongly manifested when spatially modulated transverse magnetization evolves in the presence of similarly modulated longitudinal magnetization. Such modulation can be produced by the application of RF (*7*) or magnetic field gradients (*1–5*). Previously it has been shown that signals generated in this way are sensitive to the sample structure, since the dipolar field experienced at a particular location is mainly dependent upon the surrounding magnetization found within a sphere whose radius is one "wavelength" of the modulation (with a peak sensitivity to magnetization at a distance of half a wavelength) (*6, 8*). By varying the modulation through manipulation of gradient pulse areas, structures can be probed at different length scales. In previous work, measurements were made of the average structure, in simple phantoms consisting of water surrounding polystyrene beads of known diameter (*9*). This was accomplished by analyzing the signal amplitude recorded from the whole sample as a function of the degree of modulation.

In this study, we directly demonstrate the spatial sensitivity of the dipolar signal by using it to form images of simply structured phantoms. These experiments also allow us to evaluate the mathematical expressions for the dipolar field by comparing the imaged field patterns with the results of simple simulations.

THEORY

Figure 1 shows the basic form of the CRAZED sequence (*5*) that was used as the basis of all measurements reported here. A conventional analysis of this sequence would suggest that no signal would be formed after the application of the second gradient pulse, because the gradient lobe areas are in the ratio of 1 : 2. However, the dipolar field, $\mathbf{B}_\mathrm{d}$, generated by the spatially modulated magnetization acts to refocus a fraction of the magnetization, thus producing a signal.

This signal results from the term $\frac{d\mathbf{M}}{dt} = \gamma\mathbf{M} \times \mathbf{B}_\mathrm{d}$, which is introduced into the Bloch equations by the presence of the dipolar field (*1*). For times, t, after the second RF pulse, such that $\mu_0\gamma M_0 t \ll 1$ (where M_0 is the equilibrium magnetization), this term only slightly perturbs the evolution of the magnetization. Expanding to first order and neglecting the effect of diffusion, field inhomogeneity, and relaxation, we can write the transverse magnetization, $M^+ = M_x + iM_y$ as

$$M^+(\mathbf{r}, t) \approx M^+(\mathbf{r}, 0) + i\gamma t(M_z(\mathbf{r}, 0)B_\mathrm{d}^+(\mathbf{r}) - M^+(\mathbf{r}, 0)B_{\mathrm{d}z}(\mathbf{r})), \quad [1]$$

where $B_{\mathrm{d}z}$ is the z-component of the dipolar field and $B_\mathrm{d}^+ = B_{\mathrm{d}x} + iB_{\mathrm{d}y}$ is its transverse component.

The dipolar field due to the sample magnetization, $\mathbf{M}(\mathbf{r})$, can be written as (*1*)

$$\mathbf{B}_\mathrm{d}(\mathbf{r}) = \frac{\mu_0}{8\pi^3}\int d^3k e^{i\mathbf{k}\cdot\mathbf{r}}\frac{(3(\hat{\mathbf{k}}\cdot\hat{\mathbf{z}})^2 - 1)}{2}\left(M_z(\mathbf{k})\hat{\mathbf{z}} - \frac{1}{3}\mathbf{M}(\mathbf{k})\right), \quad [2]$$

where $\mathbf{M}(\mathbf{k}) = \int d^3k e^{-\mathbf{k}\cdot\mathbf{r}}\mathbf{M}(\mathbf{r})$ is the three-dimensional spatial Fourier transform of the magnetization distribution, $\mathbf{M}(\mathbf{r})$, and $M_z(\mathbf{k})$ is similarly the Fourier transform of the z-component

1090-7807/01 $35.00

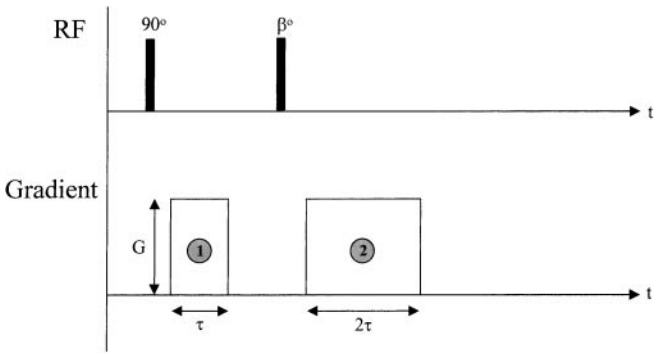

FIG. 1. The basic CRAZED sequence consisting of a 90° RF pulse followed by a gradient pulse of strength, G, and duration, τ, a β° RF pulse, and finally a second gradient pulse of the same strength, but twice the duration as the first.

of the magnetization $M_z(\mathbf{r})$. Here $\hat{\mathbf{k}} = \frac{\mathbf{k}}{|\mathbf{k}|}$, $\hat{\mathbf{z}}$ is a unit vector in the z-direction, and the term $\Lambda(\mathbf{k}) = \frac{1}{2}(3(\hat{\mathbf{k}} \cdot \hat{\mathbf{z}})^2 - 1)$ shows the characteristic symmetry of the dipolar field.

In the experiments described in this paper, we consider the situation where the magnetization is spatially modulated in the z-direction using gradient pulses whose areas can be written as nk_m, where n is an integer. This means that each component of the magnetization $M_\alpha(\mathbf{r})$, where $\alpha = x, y$, or z, can be written as a series of the form $\sum_{m=-\infty}^{m=\infty} a_{m\alpha} e^{imk_m z} M_0(\mathbf{r})$, with the $a_{m\alpha}$ being a set of constants. Using the Fourier shift theorem, the components of the spatial Fourier transform of the magnetization can be written as $\sum_{m=-\infty}^{m=\infty} a_{m\alpha} M_0(\mathbf{k} + mk_m\hat{\mathbf{z}})$, where $M_0(\mathbf{k})$ is the Fourier transform of the equilibrium magnetization distribution $M_0(\mathbf{r})$. From inspection of Eq. [2], it can be seen that this in turn means that the components of the dipolar field, $B_{d\alpha}$, take the form

$$B_{d\alpha}(\mathbf{r}) \propto \sum_{m=-\infty}^{m=\infty} e^{imk_m z} b_d(\mathbf{r}, mk_m\hat{\mathbf{z}}), \qquad [3]$$

where

$$b_d(\mathbf{r}, \boldsymbol{\kappa}) = \frac{\mu_0}{8\pi^3} \int d^3k e^{i\mathbf{k}\cdot\mathbf{r}} \Lambda(\mathbf{k} + \boldsymbol{\kappa}) \mathbf{M}_0(\mathbf{k}) \qquad [4]$$

is the spatially varying dipolar field, which we aim to image.

After application of the second gradient pulse in the sequence of Fig. 1, the components of the magnetization are described by

$$M_z(\mathbf{r}, 0) = -\sin\beta M_0(\mathbf{r}) \cos(k_m z) \qquad [5]$$

$$M^+(\mathbf{r}, 0) = -\frac{i}{2} \sin\beta M_0(\mathbf{r})((\cos\beta - 1)e^{ik_m z} + (1 + \cos\beta)e^{-ik_m z})e^{-i2k_m z}, \qquad [6]$$

where $k_m = (\gamma G \tau)$. Substituting these expressions into Eqs. [3] and [4] gives the form of the dipolar field, which can then be substituted into Eq. [1]. Following through this process we find that there are terms generated by the dipolar field which are proportional to $e^{i4k_m z}$, $e^{i2k_m z}$, and $e^{i0k_m z}$. Averaging the signal over a length L in the z-direction and assuming that the structure does not vary significantly over this length scale leaves only the term varying as $e^{i0k_m z}$. This averaging also eliminates the $M^+(\mathbf{r}, 0)$ term so that the measured signal varies as

$$M^+(\mathbf{r}, t) \approx \gamma t M_0(r) b_d(\mathbf{r}, k_m\hat{\mathbf{z}}) \sin\beta \left(\frac{\cos\beta - 1}{4}\right). \qquad [7]$$

Equation [7] indicates that the transverse magnetization is therefore proportional to the product of $M_0(\boldsymbol{r})$ and the dipolar field, $b_d(\mathbf{r}, k_m\hat{\mathbf{z}})$, and an image formed from the resulting signal will therefore display the spatial variation of the dipolar field in regions where magnetization is present.

Inspection of Eq. [4] indicates that the spatial variation of $b_d(\mathbf{r}, k_m\hat{\mathbf{z}})$ depends on the sample structure, which is encoded in $M_0(\mathbf{k})$, and on the degree of modulation, k_m. Some insight into this dependence can be obtained by considering simple, model magnetization distributions. Warren *et al*. (*5*) previously calculated the field generated at a point by surrounding spherical shells of magnetization of varying radii. Here we first consider the analogous situation in cylindrical geometry, which is of more relevance to the sample configurations used in the experiments described below. In this case, we evaluate the field generated by a cylindrical annulus of magnetization which is modulated in the z-direction at spatial frequency, k_m. The cylindrical annulus is of infinite length, radius, ρ, and infinitesimal thickness, $\delta\rho$, and is aligned with the z-direction. The variation of the field at the center of the annulus is given $\mu_0 M_0 k_m^2 \rho \delta\rho K_0(k_m\rho)$, where $K_0(x)$ is the modified Bessel function. This function, which is plotted as a function of $k_m\rho$ in Fig. 2, peaks at $k_m\rho \approx 0.6$, and

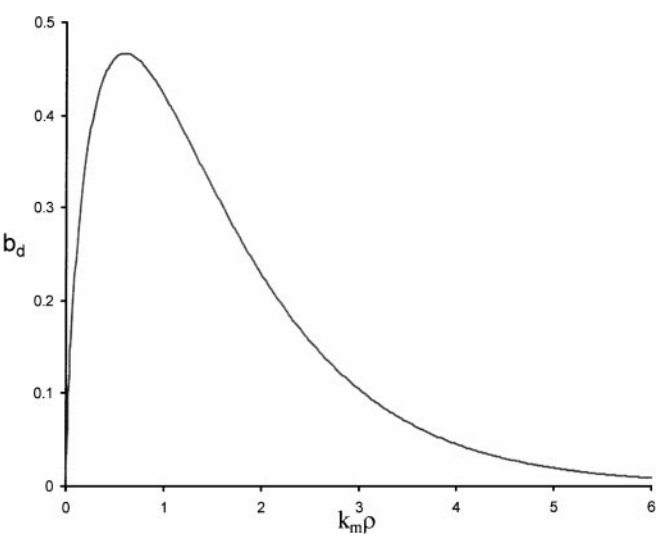

FIG. 2. The variation of the dipolar field, b_d, generated by an infinitely long annulus of modulated magnetization ($M_0 \cos(k_m z)$) of radius ρ and thickness $\delta\rho$. The field at $\rho = 0, z = 0$ is plotted in units of $\mu_0 M_0 k_m^2 \delta\rho$.

its integral with respect to ρ smoothly tends to $\mu_0 M_0$ as ρ tends to infinity, reaching 90% of the final value at $\rho \approx \pi/k_m$.This behavior, which is similar to that calculated in the spherical case (*5*), means that the dipolar field has an effective range that depends upon the length scale of modulation.

It is also worth noting that in the case of a large uniform sample, within which $M_0(\mathbf{r}) = M_0$, Eq. [4] shows that $b_d(\mathbf{r}, \kappa) = \frac{1}{2}(3(\hat{\boldsymbol{\kappa}} \cdot \hat{\mathbf{z}})^2 - 1)\mu_0 \gamma M_0$ at distances further from any boundary than k_m^{-1}, where $\hat{\kappa} = \frac{\boldsymbol{\kappa}}{|\boldsymbol{\kappa}|}$. In this situation Eq. [7] therefore predicts that the signal varies as

$$M^+(\mathbf{r}, t) \approx \mu_0 \gamma t M_0^2 \left(\frac{3(\hat{\boldsymbol{\kappa}} \cdot \hat{\mathbf{z}})^2 - 1}{2} \right) \sin\beta \left(\frac{\cos\beta - 1}{4} \right), \quad [8]$$

in agreement with previously published work (*3*).

METHODS

Experimental. Experiments were carried out at 11.7 T using a 1.5-cm-diameter bird-cage RF coil of 3.5 cm length and an actively screened gradient coil set. Two different approaches based on the CRAZED sequence were used for imaging. Figure 3 shows the sequence used for imaging samples containing a single spin species. The initial gradient encoding used to modulate the magnetization is modified so that the two pulses have areas in the ratio $1:-2$. This has the effect of picking out a signal that results from transverse magnetization originating in the second, rather than the first term in large brackets in Eq. [6]. The resulting signal therefore varies as

$$M^+(\mathbf{r}, t) \approx \gamma t M_0(r) b_d(\mathbf{r}, k_m \hat{\mathbf{z}}) \sin\beta \left(\frac{1 + \cos\beta}{4} \right), \quad [9]$$

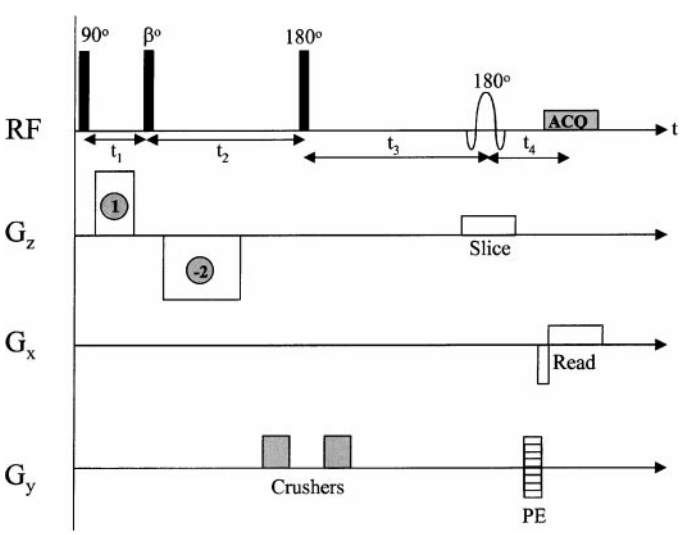

FIG. 3. The sequence used to generate images of the dipolar field pattern in samples containing a single spin species.

instead of the form given in Eq. [7]. This has the advantage of giving a maximum signal when $\beta = 60°$ rather than 120°, thus reducing sensitivity to inhomogeneities in the RF field. Imaging was performed by adding a slice-selective 180° refocusing pulse and standard spin-warp imaging gradients to the basic CRAZED sequence as shown in Fig. 3. An additional nonselective 180° pulse is used to refocus the dephasing of magnetization due to magnetic field inhomogeneities. Such a pulse fully refocuses the magnetization as long as any field inhomogeneity does not cause significant spatial modulation of the transverse magnetization on the length scale of k_m^{-1}, the pitch of the modulation induced by the gradient pulses. The relationship between pulse times which is needed to refocus the magnetization at the center of the sampling window is

$$t_3 = 2t_1 + t_2 + t_4, \quad [10]$$

while the signal grows for total time $T = t_2 + t_3 + t_4$. Although it is possible to design an imaging sequence for this type of experiment using only a single selective 180° RF pulse or by making either the first 90° or the β pulse selective (*10*), this has the effect of imposing the slice profile on the magnetization terms in Eq. [2] for approximately half or for all of the time that the signal evolves. This introduces an unwanted further spatial dependence in B_d, which is largely avoided by using the sequence of Fig. 3.

A simple $(x, y, -x, -y)$ phase cycle was applied to the first 90° RF pulse along with a receiver phase cycle $(x, -x, x, -x)$. This gives a coherent summation of the desired signal (which has a bilinear dependence on the transverse magnetization, M^+, generated after the first pulse), while canceling the contribution of standard spin echo and FID signals.

The sequence was used to generate 128 × 128 images of a 9.2-mm-inner-diameter NMR tube filled with water, mildly doped with 0.1% $CuSO_4$, using k_m values ranging from 0.7 to 8 mm^{-1}. A time for signal growth, T, of 137 ms was employed ($t_1 = 2.9$ ms, $t_2 = 60.4$ ms, $t_3 = 71.6$ ms, $t_4 = 5.4$ ms) and the initial modulation was produced in a time, $\tau = 0.3$ ms. The resolution was 90 μm, the slice thickness 6 mm, and a repetition time, $TR = 6$ s, was used.

A second sequence (Fig. 4) incorporating chemical-shift-selective RF pulses was used to generate images of the dipolar field pattern in a sample containing two spin species (Species 1 resonates at frequency ν_1, while Species 2 resonates at frequency ν_2). The first two 90° RF pulses applied at frequency ν_1 selectively affect only the magnetization of Species 1. In conjunction with the intervening gradient pulse, they generate spatially modulated z-magnetization of this species so that

$$M_{z1}(\mathbf{r}, 0) = -M_{01}(\mathbf{r}) \cos(k_m z). \quad [11]$$

The modulated transverse magnetization of Species 1 is crushed by the large gradient pulses applied immediately after the second RF pulse so that $M_1^+(\mathbf{r}, 0) = 0$. The third 90° RF

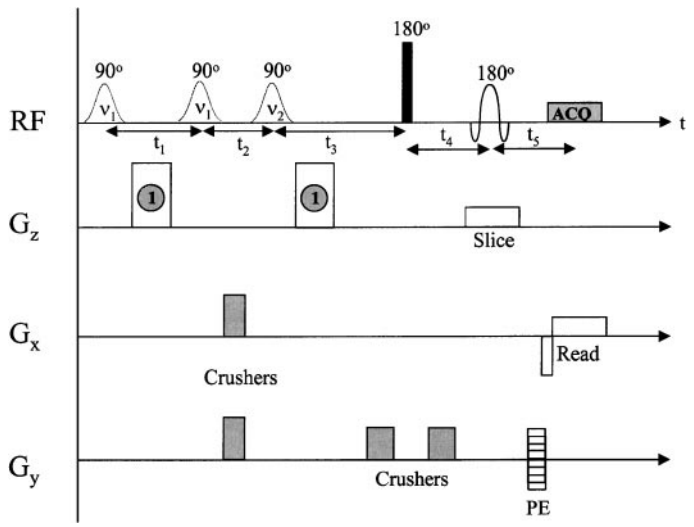

FIG. 4. The sequence used to generate images of the dipolar field in samples containing two spin species. This results in an image of the signal generated by the action of the dipolar field generated by longitudinal magnetization of Species 1 on transverse magnetization of Species 2.

pulse selectively excites Species 2 only and after the subsequent gradient pulse,

$$M_{z2}(\mathbf{r}, 0) = 0 \qquad [12]$$

$$M_2^+(\mathbf{r}, 0) = -i M_{02}(\mathbf{r}) e^{-ik_m z}. \qquad [13]$$

The dipolar field produced by M_{z1} acts to refocus a fraction of the transverse magnetization, M_2^+, giving a signal of the form

$$M_2^+(\mathbf{r}, t) \approx \frac{\gamma t}{3} M_{02}(r) b_{\mathrm{d}1}(\mathbf{r}, k_m \hat{\mathbf{z}}) \qquad [14]$$

in the limit when $\mu_0 \gamma M_{01} t \ll 1$. Here $b_{\mathrm{d}1}(\mathbf{r}, k_m \hat{\mathbf{z}})$ is the dipolar field produced by Species 1. Provided that $(\nu_1 - \nu_2) \gg \mu_0 \gamma M_{02}$, the dipolar field produced by M_2^+ does not have a coherent effect on the longitudinal magnetization of Species 2 (*4*), and no net signal is generated from this component. Imaging was performed in the same manner as for the sequence of Fig. 3, with a nonselective 180° RF pulse once again used to refocus dephasing due to magnetic field inhomogeneities. In this case, the relationship of timings needed to refocus the magnetization at the center of the gradient echo of the imaging sequence is

$$t_3 + t_5 = t_1 + t_4, \qquad [15]$$

and the signal grows for a time, $T = t_3 + t_4 + t_5$. A $(x, -x)$ phase cycle was simultaneously applied to the first and third RF pulses, along with simple (x, x) signal summation. This eliminated unwanted FID signals from the first and third pulses.

This sequence was applied to a sample consisting of two concentric tubes containing different compounds: an inner tube with an inner diameter of 4.2 mm and an outer diameter of 5 mm containing acetone (mixed with 10% D_2O containing 0.1% $CuSO_4$, so as to reduce the T_1 relaxation time and eliminate dielectric resonance effects (*11*)) and an outer tube of 9.2 mm inner diameter containing water, doped with 0.1% $CuSO_4$. The frequency difference between the ^{1}H nuclei in the acetone CH_3 groups and in the water was 980 Hz, allowing for the effect of bulk magnetic susceptibility shifts (*12*). Images were generated of the acetone signal produced by modulating the longitudinal magnetization of the water and of the water signal generated by modulating the longitudinal magnetization of the acetone. This allowed investigation of the dipolar field pattern produced outside the region containing the responsible magnetization.

We acquired 128 × 128 images, with 120 μm in-plane resolution and 6 mm slice thickness, using a *TR* of 6 s. Gaussian RF pulses (3.68 ms duration, 1.95 ms FWHM) were used for chemical shift selection. Modulation was generated using gradient pulses of length 1.2 ms and the time over which the signal grew was 107 ms, with $t_1 = 7.2$ ms, $t_2 = 12.7$ ms, $t_3 = 52.5$ ms, $t_4 = 50$ ms, and $t_5 = 4.7$ ms.

Simulations. The expected pattern of signal variation was calculated for the two sample configurations using Eq. [4]. This requires an expression for $M_0(\mathbf{k})$, which for an infinite cylinder of uniform magnetization, m_0, with radius, a, is given by

$$M_0(\mathbf{k}) = m_0 a^2 \frac{J_1(k_\rho a)}{k_\rho a} \delta(k_z), \qquad [16]$$

while for an infinitely long annulus of inner radius, a, and outer radius, b, as formed in the sample comprising two concentric tubes,

$$M_0(\mathbf{k}) = m_0 \left[b^2 \frac{J_1(k_\rho b)}{k_\rho b} - a^2 \frac{J_1(k_\rho a)}{k_\rho a} \right] \delta(k_z). \qquad [17]$$

In both expressions, δ is the Dirac delta function, whose presence along with the azimuthal symmetry means that the integral over $\mathbf{k}$ in Eq. [4] only has to be evaluated over k_ρ, the radial coordinate in k-space. In reality, the extent in the z-direction of the contributing $M_0(\mathbf{r})$ is defined by the RF coil homogeneity, and the function $\delta(k_z)$ should be replaced by a broader function, whose width will be proportional to l^{-1}, where l is the length of the coil's homogeneous volume. The approximate length of the homogeneous volume of the bird-cage coil used in these experiments was 2.5 cm. For the range of modulation frequencies, k_m, used here, this means that the finite sample extent is likely to have had some effect on the signal measured at the lowest k_m values ($k_m l \sim 6\pi$).

RESULTS

Figure 5 shows images of the single tube of doped water obtained using k_m values of 4.73, 2.36, 0.95, and 0.71 mm^{-1} (corresponding values of the pitch of modulation, $2\pi/k_m$, are

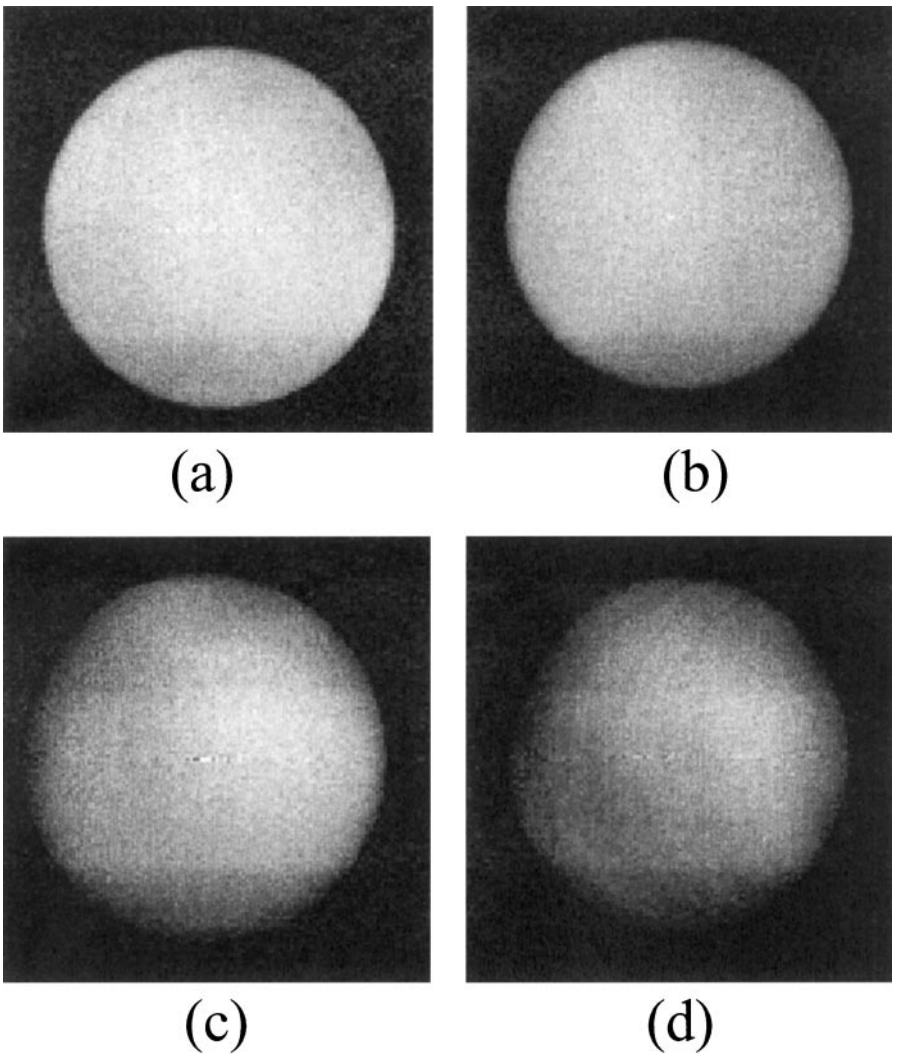

FIG. 5. 128×128 ($90 \times 90 \times 6000$ μm^3 voxel size) images of a 9.2-mm-inner-diameter tube containing water, generated using the sequence shown in Fig. 3. The following values of k_m were employed: (a) 4.73 mm^{-1}; (b) 2.36 mm^{-1}; (c) 0.95 mm^{-1}; (d) 0.71 mm^{-1}.

1.4, 2.7, 6.6, and 8.8 mm), with the sequence of Fig. 3. Corresponding simulations, which were calculated using Eqs. [4] and [16], are shown in Fig. 6. Figure 7 shows the radially averaged variation of the signal with radius for both the image data (a) and simulations (b). These data show that the field is uniform in the sample center, but decreases in magnitude in a region at the outer radius of the tube whose width increases in size with decreasing k_m. The reduction in signal is a consequence of the reduced amount of local magnetization in the region near the circumference of the sample. This results in a weakened dipolar field when all field contributions shown in Fig. 2 are summed. Viewed in the k-domain, $\Lambda(\mathbf{k} + k_m\hat{\mathbf{z}})$ acts as a k-space filter, modifying the contributions of the spatial frequencies that make up $M_0(r)$, in a manner that depends on the magnitude of k_m. As Fig. 8 shows, with $a = 4.6$ mm the filter hardly modifies $M_0(\mathbf{k})$ at $k_m = 4.73$ mm^{-1}, while at $k_m = 0.71$ mm^{-1}, there is a significant modification of $M_0(\mathbf{k})$ at high spatial frequencies. The image obtained at high k_m therefore follows $M_0(\mathbf{r})$, while that gathered at low k_m shows edge attenuation.

Although the images of Figs. 5 and 6 show good qualitative agreement between the experimentally measured and the calculated dipolar field patterns, there are significant differences in the form of the radial average data shown in Fig. 7. These mainly result from the effect of RF inhomogeneity, which the sequences of Figs. 3 and 4 are particularly sensitive to, as a consequence of the large number of RF pulses they employ and the fact that the measured signal depends upon a product of transverse and longitudinal magnetization terms, both of which are affected by imperfection in each pulse. This effect can be most clearly seen in the significant radial variation of the signal at small radii in the experimental data gathered at the highest k_m values. Other effects that have not been considered in the simulations are those of radiation damping, the finite effective sample length, and magnetic field inhomogeneity. Incomplete cancellation

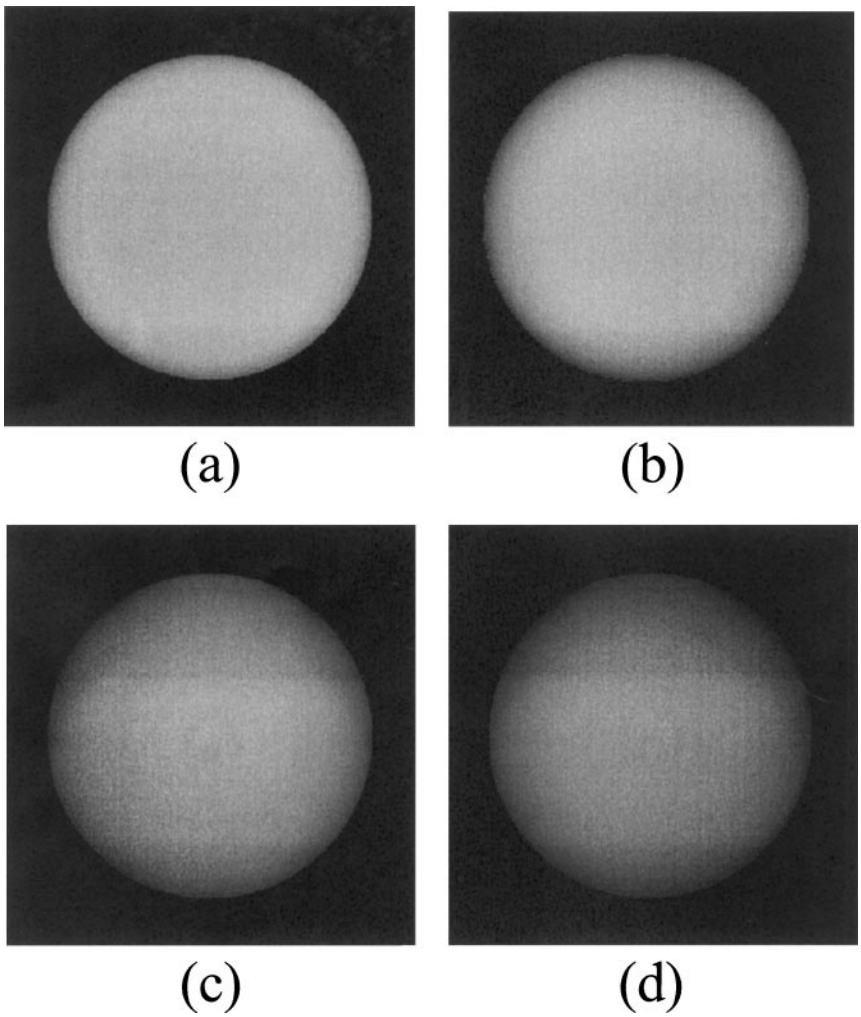

FIG. 6. Simulated images corresponding to the imaging parameters of Fig. 5.

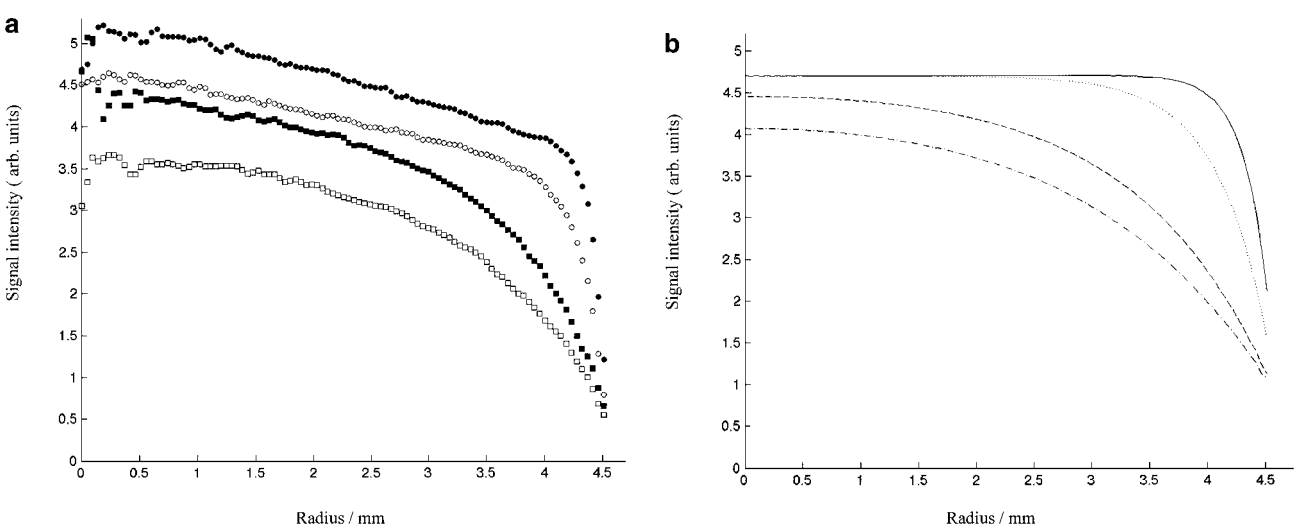

FIG. 7. Variation of average signal intensity with radius in the images of Figs. 5 and 6. (a) Experimental data: closed circles, 4.73 mm^{-1}; open circles, 2.36 mm^{-1}; closed squares, 0.95 mm^{-1}; open squares, 0.71 mm^{-1}. (b) Simulated data: continuous line, 4.73 mm^{-1}; dotted line, 2.36 mm^{-1}; dashed line, 0.95 mm^{-1}; dot–dashed line, 0.71 mm^{-1}.

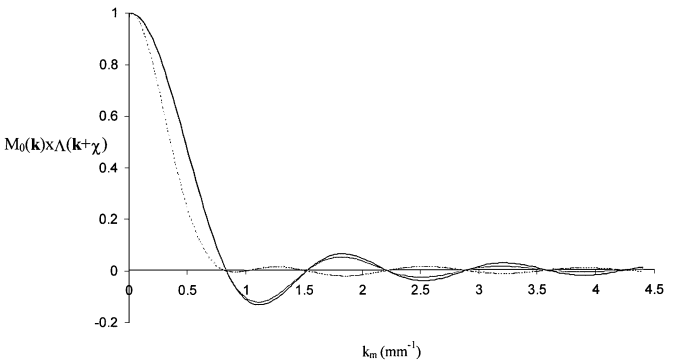

FIG. 8. Calculated variation of $M_0(\mathbf{k})\Lambda(\mathbf{k}+\boldsymbol{\kappa})$ with k_ρ for varying values of $\boldsymbol{\kappa} = k_m\hat{\mathbf{z}}$: continuous dark line, $k_m = \infty$ mm^{-1}; continuous gray line, $k_m = 4.73$ mm^{-1}; dashed line, $k_m = 0.71$ mm^{-1}. $M_0(\mathbf{k})$ is given by Eq. [16], with $a = 4.6$ mm.

of the signal from the terms varying as $e^{\pm ik_m z}$, $e^{i4k_m z}$, and $e^{i2k_m z}$, which is more likely to occur with weaker modulation, also causes artifacts in the images.

Figure 9 shows images generated using the sequence of Fig. 4, in which water acts as Species 1 and the acetone as Species 2. The k_m values used were 15.9, 3.97, 2.38, and 1.19 mm^{-1}. Corresponding simulations are shown in Fig. 10. Figure 11 shows experimental and simulated images that were produced with the roles of the water and acetone reversed and $k_m = 2.38$ mm^{-1}. It can be seen from the experimental data that the signal mainly results from Species 2 magnetization in the region which is closest to Species 1, i.e., at the outer extreme of the inner tube in Fig. 9, or at the inner extreme of the outer annulus in Fig. 11a. The extent of the signal-contributing region in Fig. 9 increases as the modulation is reduced, as would be expected from the

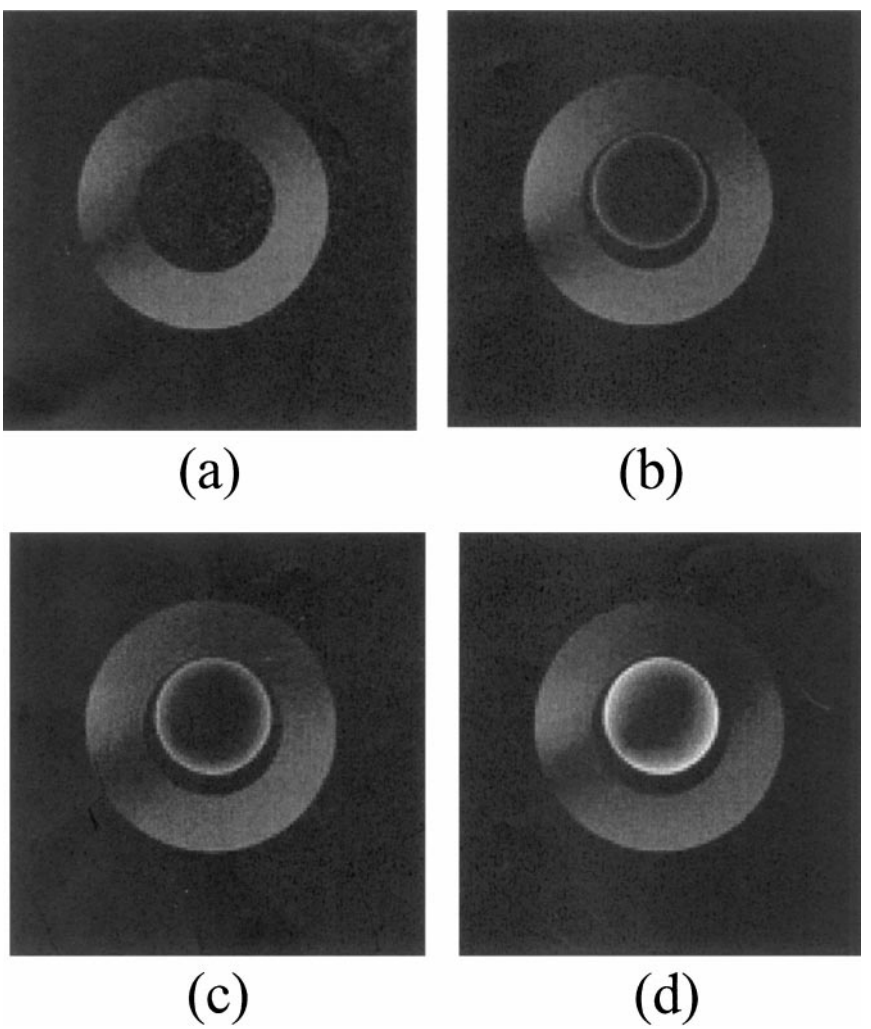

FIG. 9. 128 × 128 (120 × 120 × 6000 μm^3 voxel size) images of a sample consisting of a tube containing acetone (4.1 mm id, 5 mm od) inside a tube containing water (9.2 mm id). These were generated using the sequence shown in Fig. 4, with water acting as Species 1 and acetone as Species 2. The following values of k_m were employed: (a) 15.9 mm^{-1}; (b) 3.97 mm^{-1}; (c) 2.38 mm^{-1}; (d) 1.19 mm^{-1}.

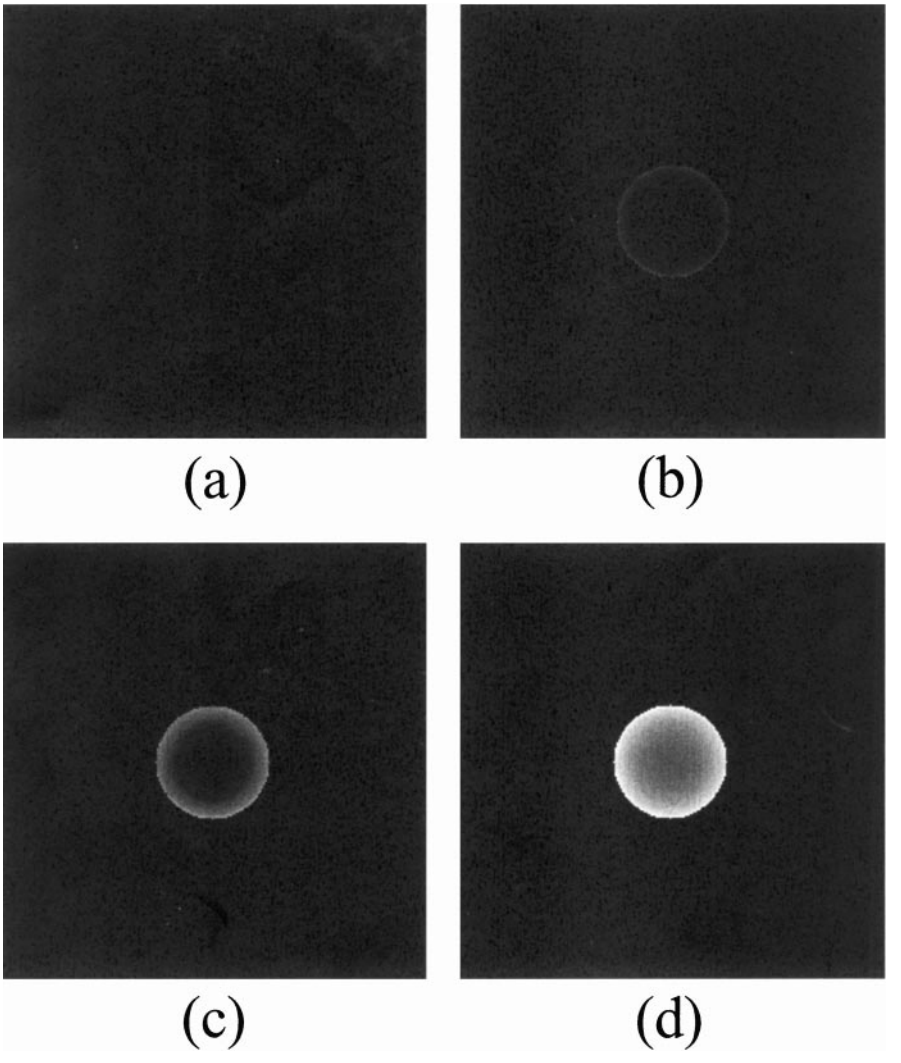

FIG. 10. Simulated images corresponding to the imaging parameters of Fig. 9.

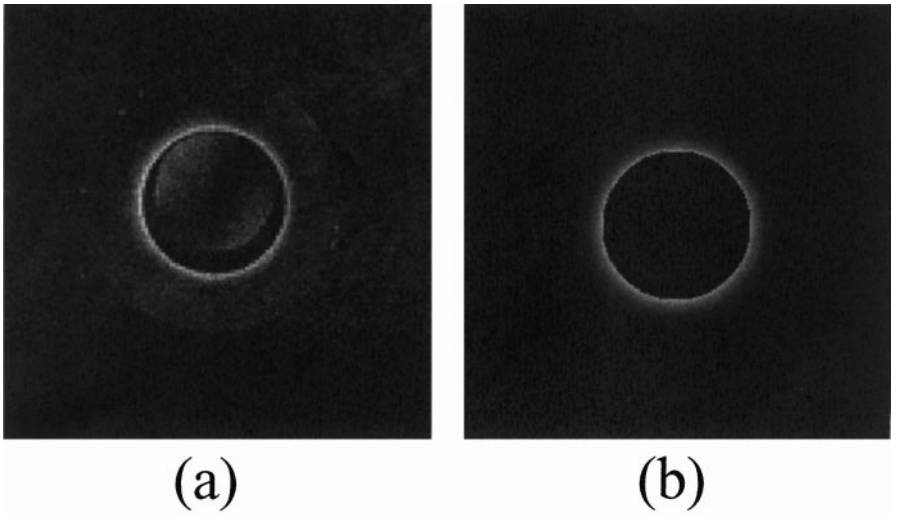

FIG. 11. Experimentally generated (a) and simulated (b) 128 × 128 (120 × 120 × 6000 μm^3 voxel size) images of a sample consisting of a tube containing acetone (4.1 mm id, 5 mm od) inside a tube containing water (9.2 mm id) with $k_m = 2.38$ mm^{-1}. These were generated using the sequence shown in Fig. 4, with acetone acting as Species 1 and water as Species 2.

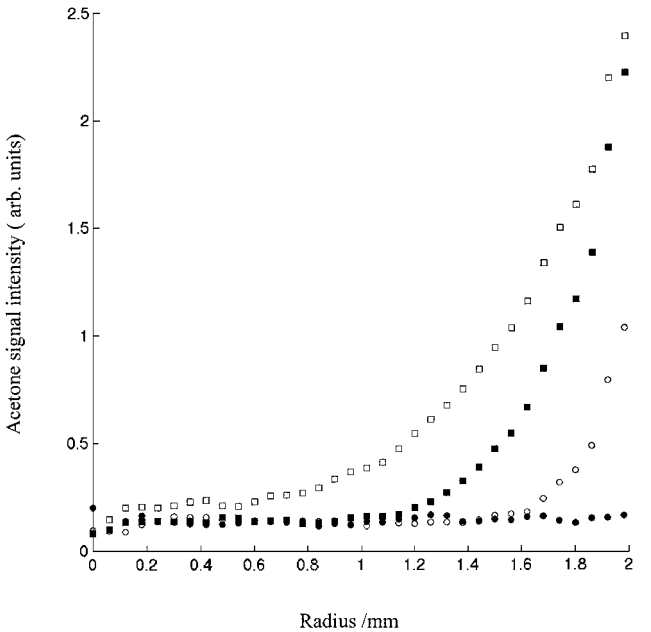

FIG. 12. Variation of average acetone signal intensity with radius in the images of Fig. 9. Experimental data: closed circles, 15.9 mm^{-1}; open circles, 3.97 mm^{-1}; closed squares, 2.38 mm^{-1}; open squares, 1.19 mm^{-1}.

scaling of the range of the dipolar field with k_m^{-1}. This behavior is reproduced in the simulations. In both sets of experimentally generated images there is some weak signal from Species 1. This is a consequence of stimulated echo signal generated by the third RF pulse from the spatially modulated longitudinal magnetization produced by the first pair of RF pulses. The final pulse should only excite Species 2 magnetization, but its frequency response is broad enough to also weakly excite Species 1. The resulting signal is shifted by three pixels in the read (vertical) direction due to the chemical shift difference, but does not overlap with that from Species 2 and so does not interfere with the measured dipolar field pattern. Figure 12 shows the variation of the radially averaged acetone signal from the images of Fig. 9 for different modulations. It confirms the increase in the range of the dipolar field from the outer water annulus as the modulation frequency is reduced.

CONCLUSIONS

The images shown here directly demonstrate the spatial sensitivity of NMR signals generated from the nuclear dipolar field due to spatially modulated magnetization. They also show that the length scale over which the field acts depends upon the degree of spatial modulation. The measured signal patterns correspond well with simulated data, calculated from simple expressions based on the local relationship between the dipolar field and the magnetization in the Fourier domain (*1*). While it is probably more likely that *imaging* experiments based on the use of the dipolar field (*10, 13*) will find applications in other areas, such as functional imaging (*14*) or mapping M_0 (*15*), than in structure measurements, the work described here provides useful verification of the structural sensitivity reported in previous measurements on bulk samples. Such measurements of average structure may have useful applications in the study of emulsions, porous media, and heterogeneous biological samples (*16*).

REFERENCES

1. G. Deville, M. Bernier, and J. M. Delrieux, NMR multiple echoes observed in solid ^{3}He. *Phys. Rev. B* **19,** 5666 (1979).
2. D. Einzel, G. Eska, Y. Hirayoshi, T. Kopp, and P. Wolfle, Multiple spin echoes in a normal Fermi-liquid. *Phys. Rev. Lett*. **53,** 2312–2315 (1984).
3. R. Bowtell, R. M. Bowley, and P. Glover, Multiple echoes in a liquid in a high magnetic field. *J. Magn. Reson*. **88,** 643–651 (1990).
4. A. S. Bedford, R. Bowtell, and R. M. Bowley, Multiple spin echoes in multicomponent liquids, *J. Magn. Reson*. **93,** 516–532 (1991).
5. W. S. Warren, W. Richter, A. H. Andreotti , and B. T. Farmer, Generation of impossible cross-peaks between bulk water and biomolecules in solution NMR. *Science* **262,** 2005–2009 (1993).
6. W. Richter, S. Lee, W. S. Warren, and Q. He, Imaging with intermolecular multiple-quantum coherences in solution nuclear-magnetic-resonance. *Science* **267,** 654–657 (1995).
7. A. Jeerschow, Multiple echoes initiated by a single radio frequency pulse in NMR, *Chem. Phys. Lett*. **296,** 466–470 (1998).
8. R. Bowtell and P. Robyr, Structural investigations with the dipolar demagnetising field in solution NMR. Phys. *Rev. Lett*. **76,** 4971–4974 (1996).
9. P. Robyr and R. Bowtell, Nuclear magnetic resonance microscopy in liquids using the dipolar field. *J. Chem. Phys*. **106,** 467–476 (1997).
10. W. S. Warren, S. Ahn, M. Mescher, M. Garwood, K. Ugurbil, W. Richter, R. Rizi, J. Hopkins, and J. S. Leigh, MR imaging contrast enhancement based on intermolecular zero quantum coherences. *Science* **281,** 247–251 (1998).
11. S. Crozier, I. M. Brereton, F. O. Zelaya, W. U. Roffmann, and D. M. Doddrell, Sample-induced RF perturbations in high-field, high-resolution NMR spectroscopy. *J. Magn. Reson*. **126,** 39–47 (1997).
12. S. C-K. Chu, Y. Xu, J. A. Balschi, and C. S. Springer, Bulk magnetic susceptibility shifts in NMR studies of compartmentalised samples: use of paramagnetic reagents. *Magn. Reson. Med*. **13,** 239–262 (1990).
13. J. H. Zhong, Z. Chen , and E. Kwok, In vivo intermolecular double-quantum imaging on a clinical 1.5 T MR scanner. *Magn. Reson. Med*. **43,** 335–341 (2000).
14. W. Richter, M. Richter, W. S. Warren, H. Merkle, P. Andersen, G. Adriany, and K. Ugurbil, Functional magnetic resonance imaging with intermolecular multiple-quantum coherences. *Magn. Reson. Imag*. **18,** 489–494 (2000).
15. S. Gutteridge, C. Ramanathan, and R. Bowtell, Mapping the absolute value of M_0 using dipolar field effects, Abstracts of the ISMRM 8thAnnual Meeting, Denver, p. 268 (2000).
16. S. Capuani, F. Curzi, B. Maraviglia, and A. Bifone, Multiple spin echo NMR imaging for the evaluation of trabecular bone quality. Proceedings of the 30th Congress Ampere, Lisbon, p. 19 (2000).